Article

Microwave-Assisted Synthesis of rGO-ZnO/CuO Nanocomposites for Photocatalytic Degradation of Organic Pollutants

Aklilu Guale Bekru [1], Lemma Teshome Tufa [1,2], Osman Ahmed Zelekew [3,*], Juyong Gwak [4], Jaebeom Lee [2,4] and Fedlu Kedir Sabir [1,*]

1   Department of Applied Chemistry, Adama Science and Technology University, Adama P.O. Box 1888, Ethiopia
2   Research Institute of Materials Chemistry, Chungnam National University, Daejeon 34134, Republic of Korea
3   Department of Materials Science and Engineering, Adama Science and Technology University, Adama P.O. Box 1888, Ethiopia
4   Department of Chemistry, Chemistry Engineering and Applied Chemistry, Chungnam National University, Daejeon 34134, Republic of Korea
*   Correspondence: osman.ahmed@astu.edu.et (O.A.Z.); fedluked130@gmail.com (F.K.S.)

Abstract: Nanomaterial-based catalytic conversion of hazardous organic pollutants into benign substances is one of the green methods employed for wastewater treatment. This study demonstrates the fabrication of (rGO-ZnO)/CuO nanocomposites (NCs) via a microwave (MW)-assisted method for (photo)catalytic application. The crystal structure, optical, morphological, and electrochemical characteristics were examined using X-ray diffraction (XRD), spectroscopic, microscopic, and electrochemical techniques. The analysis indicated that rod-like (rGO-ZnO)/CuO NCs having a nanoscale diameter with enhanced light absorption and well-matched band positions between rGO-ZnO and CuO were formed. Furthermore, the catalytic reduction of 4-nitrophenol (4-NP) and photocatalytic degradation of methylene blue (MB) tests showed remarkable results with rate constants of 0.468 min^{-1} for 4-NP reduction within 8 min and 0.02213 min^{-1} for MB degradation within 105 min. Thus, the artful decoration of ZnO nanorods (NRs) with CuO into the (rGO-ZnO)/CuO NCs interface is an effective strategy for fabricating highly efficient photocatalysts.

Keywords: p-n heterojunctions; (rGO-ZnO)/CuO nanocomposites; nanorods; photocatalysis; catalytic reduction

1. Introduction

Nowadays, nanostructured materials have been acquiring significant attention for applications in environmental remediation [1–4]. Specifically, heterogeneous photocatalysts have been recognized as a promising method for degrading organic water pollutants [5]. Organic pollutants, for instance, dyes from untreated textile industry effluents, can cause serious health and environmental problems [6,7]. More specifically, MB and 4-NP are among the major industrial pollutants discharged into water bodies, causing toxicity, vomiting, nausea, and eye irritation, among others [8,9]. Therefore, their removal is vital. In this regard, the use of nanomaterials for photocatalytic degradation has an advantage over other conventional methods to remove organic dyes due to their green properties, simplicity, and affordability, among others [10,11]. Generally, catalysis experiments for waste water remediation require mild conditions and simple UV–vis spectroscopy techniques to monitor the reaction/degradation progress, making catalysis a facile, eco-friendly, economical, and flexible approach [12,13].

In the field of photocatalysis, metal oxides and metal oxide-based nanostructured materials have drawn considerable attention due to their distinctive properties [14]. Among these oxides, ZnO has been extensively studied because of its impressive properties. Wide

bandgap, affordability, high binding energy, and availability as well as ease of preparation are some of the features that make an n-type ZnO a highly relevant material for photocatalysis [15,16]. However, the practical applications of pristine ZnO were limited due to the high rate of e^-/h^+ recombination, the wide bandgap for the activation by visible light, and the photocorrosion in aqueous media [15,17]. Studies have shown that coupling ZnO with readily available, nontoxic, low-bandgap p-type semiconductor CuO greatly improved visible light absorption capacity, e^-/h^+ recombination rates, and degree of photostability in aqueous media [18–20]. Nevertheless, adsorption capacity, recoverability, as well as reusability are still limiting the large-scale application of p-n heterojunction of CuO-ZnO for photocatalytic remediation of organic pollutants. According to the literature reports, using carbonaceous nanomaterials (graphene, carbon nanotubes, etc.) as catalyst support increases the adsorptivity, reduces photocorrosion, and improves the dispersibility of the resulting nanocomposites (NCs) in aqueous media [21–23]. High electrical conductivity, large surface area, and 2D structure make graphene the most suitable catalyst-support material [24]. It is therefore highly desirable to prepare CuO-ZnO–graphene NCs for promising heterogeneous photocatalysis.

The photocatalytic activity of nanomaterials is highly morphology-dependent. Owing to their morphology, 1D nanostructures exhibit attractive features that make them a potential candidate for photocatalytic applications [25]. In particular, ZnO nanorods (NRs) are known for having high surface area and aspect ratio, fast charge transfer, high photosensitivity, better charge separation, and efficient confinements on electrons and photons [26–28]. Liu et al. have reported that ZnO NRs possess better photocatalytic activities (99.8%) than truncated hexagonal cones (75%) and multilayered disks (23%) against methyl orange under UV irradiation [29]. Hence, designing an effective technique to synthesize a rod-like (rGO-ZnO)/CuO nanostructure is highly desirable to exploit the maximum benefit from its catalytic applications.

Recently, nanostructures comprised of ZnO, rGO, and CuO components with varieties of morphologies were reported for catalytic applications. These include flower-like for photocatalytic degradation of RhB and 4-chlorophenol [21], needle-like for photocatalytic oxidation of flue gas [30], flower-rod-like heterostructures for 4-nitroaniline catalytic reduction [31], and others [32]. Generally, the synthesis methods reported in most cases involve the co-deposition of both ZnO and CuO on rGO or GO sheets. Among the synthesis methods reported are solid-state [21], hydrothermal [30–34], wet chemical/ refluxing [35], and other methods [36,37]. Inherent to the attractive features of nanorods, reports on the synthesis of rod-shaped (rGO-ZnO)/CuO for MB degradation and 4-NP reduction are rare. Impregnation of the preformed rGO-ZnO nano seed with Cu^{2+} in the presence of polyethylene glycol (PEG) facilitates the growth of the nano-seeds into a rod-shaped multi-heterojunction (rGO-ZnO)/CuO NCs under microwave (MW) irradiation. MW irradiation offers higher reproducibility, purity, yields, and scalability as compared to conventional methods [38,39].

In this context, the purpose of this work is, therefore, to synthesize a novel (rGO-ZnO)/CuO NRs catalyst by MW-assisted method for organic water pollutants removal applications. The optical characteristics, crystal structures, morphology, and composition of the synthesized material were investigated. The (rGO-ZnO)/CuO NCs performance was tested against MB photocatalytic degradation and 4-NP catalytic reduction.

2. Materials and Methods

2.1. Materials

Graphite powder (C) (Blulux, 99.5%), zinc acetate $(Zn(CH_3COO)_2.2H_2O)$ (UNI-CHEM, 99%), copper (II) nitrate $(Cu(NO_3)_2.3H_2O)$ (UNI-CHEM, 99%), potassium permanganate $(KMnO_4)$ (alpha, 99.5%), sulfuric acid (H_2SO_4) (Loba, 98%), orthophosphoric acid (H_3PO_4), (Loba, 75%), sodium borohydride $(NaBH_4)$ (SRL, 95%), ascorbic acid $(C_6H_8O_6)$ (SRL, 99%), sodium hydroxide (NaOH) (Loba, 98%), polyethylene glycol 200 (Loba), concentrated hydrochloric acid (HCl) (Loba, 35.4%), methylene blue $(C_{16}H_{18}ClN_3S.3H_2O)$, and hydrogen

peroxide (H_2O_2) (Fine chemicals, 30%) were used. Distilled water (DW) was used for washing and solution-preparation purposes.

2.2. Method

2.2.1. Synthesis of GO

GO was synthesized using improved Hammer's method with few modifications [40]. Briefly, 1 g graphite powder and 160 mL mixture of H_2SO_4/H_3PO_4 (volume ratio 9:1) were mixed in the ice bath under magnetic stirring. After 30 min of stirring, 6 g of $KMnO_4$ was slowly added to the mix keeping the temperature below 10 °C using the ice bath. After that, the whole content was stirred overnight at a temperature between 35 °C to 40 °C. To the resulting mixture, 100 mL DW was added slowly under stirring. Then, an additional 100 mL of DW was added instantly. Eventually, 5 mL H_2O_2 was added to the mixture and stirred for 10 min, which resulted in a yellowish solution. The yellow suspension was left overnight to stand still. The supernatant was decanted away, and the residue was washed repeatedly with DW and finally with ethanol. The resulting brown residue was dried at 60 °C for 12 h.

2.2.2. Synthesis of rGO

Ascorbic acid was used to reduce graphene oxide according to the procedure described elsewhere with some modifications [41]. GO dispersion (0.2 mg/mL) was prepared in water and ethanol mix (with 8:2 volume fraction H_2O/CH_3CH_2OH) utilizing ultrasonication for 1 h. To the resulting 400 mL dispersion, 1.2 g of ascorbic acid was added and stirred for 20 min. The pH of the medium was adjusted to 10 by NaOH (20 wt%) aqueous solution. Then, the mixture was subjected to MW irradiation for 15 min at 50% of the 1000-watt output power oven. Subsequently, the black suspension was left to stand still for 6 h to settle the rGO. To purify the resulting product, the residue was filtered and washed well with water repeatedly until the filtrate pH reached 7 and then with ethanol. In the end, the residue was dried for 12 h at 80 °C.

2.2.3. Synthesis of (rGO-ZnO)/CuO NCs

The (rGO-ZnO)/CuO NCs were synthesized according to the following procedure. First, 80 mg rGO was dispersed in a 150 mL mixture of DW and ethanol in a 2:8 ratio under sonication for 30 min. To this dispersion, 50 mL of 0.225 M $Zn(CH_3COO)_2.2H_2O$ was added and then stirred for 20 min at 70 °C. Then, the pH was adjusted to 10 by NaOH (20 wt%) [42]. The resulting greyish-white suspension was put in the microwave oven and irradiated for 10 min at 50% of the 1000-watt output power oven. After cooling, the content was stirred for 20 min at 70 °C. To this suspension, 12 mL ($Cu(NO_3)_2.3H_2O$) (0.225 M) and 10 mL polyethylene glycol (PEG-200) were added drop by drop. NaOH was used to adjust the pH to 10. The resulting greyish solution was further MW irradiated for 10 min. Finally, the resulting precipitate was washed with ample water and then with ethanol. Drying was carried out at 80 °C for 6h and then at 200 °C for 2 h. For comparison, CuO-ZnO NCs and ZnO NPs were prepared. Hence, the same route as that of (rGO-ZnO)/CuO was followed: (i) without the addition of GO (to prepare CuO-ZnO) and (ii) without the addition of GO and $Cu(NO_3)_2.3H_2O$ (to prepare ZnO). The products obtained were then used for characterization and catalytic degradation and reduction of pollutants. Scheme 1 shows the synthesis overview of (rGO-ZnO)/CuO.
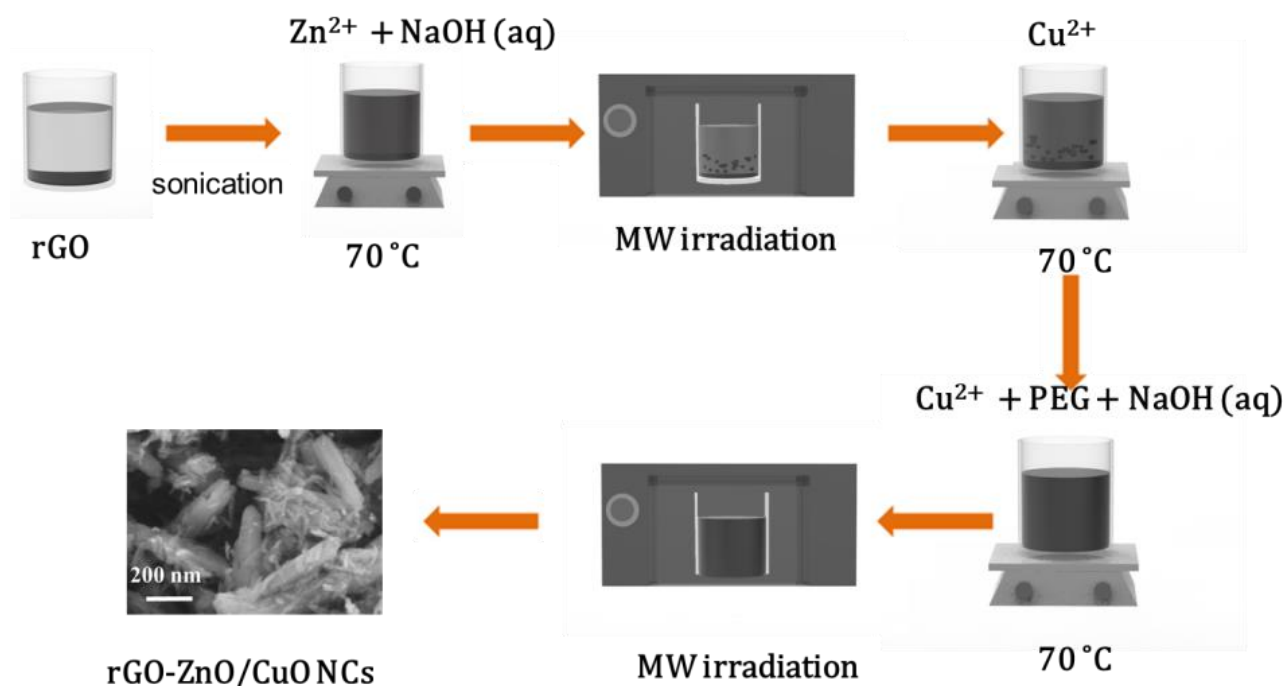
Scheme 1. Diagrammatic illustration of (rGO-ZnO)/CuO NCs synthesis by MW-assisted method.

2.3. Characterizations

To investigate the crystallinity and structural phases of the samples, an X-ray diffraction (XRD) instrument (XRD-7000S, Shimadzu, Kyoto, Japan) with Cu Kα radiation was used. A UV–vis spectrophotometer (Azzota: SM-1600, Hyderabad, India) was used to determine the UV–vis absorbance spectrum. Similarly, FTIR spectral characterization of the samples was performed using Spectrum 65 FT-IR (Perkin Elmer, Waltham, MA, USA) in the range 4000–400 cm^{-1} using KBr pellets. Scanning electron microscopy (SEM) (HITACHI, S-4800, Tokyo, Japan) was employed to analyze the surface morphology of the samples and the elemental mapping of the species found in the sample. The emission spectra of the samples were obtained by a fluorescence spectrophotometer (Agilent Cary Eclipse Fluorescence Spectrophotometer, Santa Clara, CA, USA). The electrochemical measurements were conducted using the Ivium Technologies system with an IviumSoft (v4.1018) and a standard three-electrode cell with Ag/AgCl reference electrode (saturated), platinum wire counter electrode, and FTO coated with the catalyst sample as working electrode.

2.4. Performance Evaluation

Photocatalytic performance of the (rGO-ZnO)/CuO sample was tested against the MB degradation (with a 150-watt tungsten-halogen lamp, Philips). First, 120 mL of MB (10 ppm) and 20 mg catalyst were used to prepare the reaction suspension. The catalyst and dye molecules were homogenously dispersed by sonication for 30 min. While stirring, the mixture was irradiated by visible light. The progress of degradation was monitored by withdrawing 4 mL sample every 15 min and recording the absorbance. After filtration, the absorbance of each sample was measured. The trapping experiment was carried out similarly to the MB photodegradation using 20 mg (rGO-ZnO)/CuO NCs, 1 mmol scavenger, and 120 mL of 10 ppm MB. Equations (1) and (2) were used to determine degradation percentage (D%) and reaction rate, respectively [23].

$$D(\%) = \frac{C_0 - C_t}{C_0} \times 100 \qquad (1)$$

$$\ln\left(\frac{C_t}{C_o}\right) = -kt \tag{2}$$

where k stands for the rate constant, and C_0 and C_t stand for concentrations before (or at time = 0 min) and after exposure to light (or at time = t min), respectively.

To evaluate the catalytic performance of the prepared samples, 4-NP was used as a model pollutant along with $NaBH_4$ as a reductant. Typically, a 40 mg catalyst sample and 40 mg $NaBH_4$ were mixed with 100 mL of 20 ppm 4-NP in a 250 mL beaker. The progress of catalysis was determined by a UV–vis spectrophotometer [43]. The absorbance spectrum of the solution was recorded every 3 min by withdrawing 3 mL out of the mixture. Finally, Equation (2) was used to analyze the rate of reduction.

3. Results and Discussion

3.1. X-ray Diffraction Analysis

The information about the crystalline structure and phase composition of the synthesized materials was obtained from the XRD analysis. The XRD pattern of GO, rGO, ZnO, CuO-ZnO, and (rGO-ZnO)/CuO samples are displayed in Figure 1A. The characteristic XRD peaks of GO and rGO were displayed at 2θ of 9.9° and 24.4°, with a corresponding interlayer distance of about 0.89 nm and 0.36 nm, as shown in Figure 1A. The relatively wider interlayer distance of GO could be attributed to the presence of carboxyl, hydroxyl, and epoxide groups formed by the oxidation of the graphite [44–46], whereas the reduction of GO to rGO resulted in an interlayer distance decreased to about 0.3640 nm, which is closer to that of the literature values for bulk graphite, suggesting the reduction of the hydroxyl, carboxyl, and epoxide functional groups [45,46]. Further, the peak at 2θ of 9.9° was absent, while the new peak at 2θ of 24.4° also indicates the reduction of the oxygen-containing functional groups.
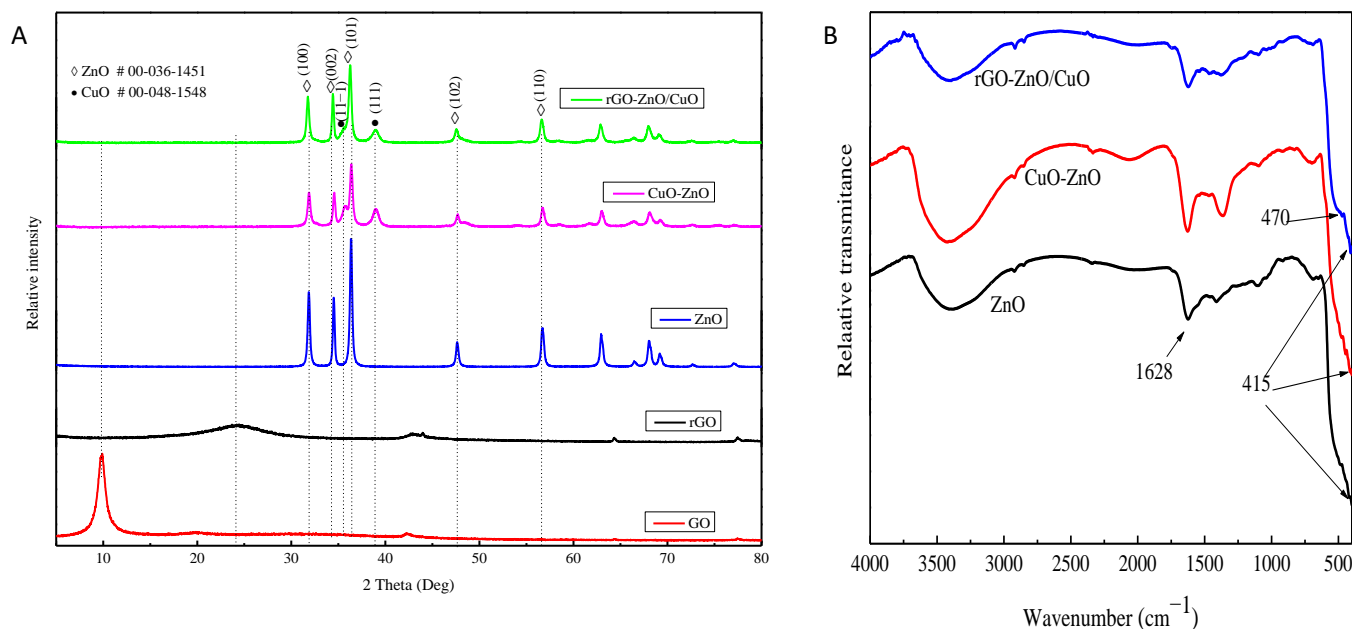

Figure 1. (**A**) XRD patterns of GO, rGO, ZnO, CuO-ZnO, and (rGO-ZnO)/CuO samples; (**B**) FTIR spectra of ZnO, CuO-ZnO, and (rGO-ZnO)/CuO samples.

As illustrated in Figure 1A, the diffraction patterns of (rGO-ZnO)/CuO appeared at 2θ of (31.76, 34.42, 36.26, 47.56, 56.62, 62.88, and 67.98°), which could be from (100), (002), (101), (102), (110), (103), and (112) planes of hexagonal ZnO phases according to JCPDS card (36-1451), respectively. Most of the diffraction peaks arising from CuO were weak and masked by strong peaks from the ZnO phase related to the relatively smaller CuO

content. Hence, the weak diffraction peaks appeared at 2θ of (35.54, 38.90, 58.26, and 61.52°) assigned to planes ((11-1), (200), (202), and (11-3)) belonging to the monoclinic CuO phases according to JCPDS card (36-1451), respectively. Distinct peaks related to the rGO were not seen in the pattern of (rGO-ZnO)/CuO, which might be due to the low crystallinity and small amount of rGO producing low intensity [44,47].

3.2. FTIR Analysis

To investigate the metal–oxygen linkage of the prepared materials, the FTIR analysis was conducted, and the resulting spectra of the ZnO, CuO-ZnO, and (rGO-ZnO)/CuO are given in Figure 1B. The bands at 3422 and 1300 cm^{-1} correspond to the O–H groups stretching and bending vibrational frequencies, respectively. Similarly, the peak at 1628 cm^{-1} could be ascribed to the C=O bond stretching [48]. The source of the O-H and C=O functional groups could be due to the adsorbed H_2O and CO_2 molecules during sample preparation. The M-O stretching vibrations of metal oxides usually appear in the ranges between 400 and 600 cm^{-1} of the FTIR spectrum. In light of this, the peaks that appeared in the range 400–510 cm^{-1} (Figure 1B) could belong to the Cu–O and Zn–O vibrations of CuO and ZnO samples, respectively [49]. The pristine ZnO sample displayed a peak at 415 cm^{-1} corresponding to Zn-O vibrations [50]. Similarly, the CuO-ZnO and (rGO-ZnO)/CuO samples showed peaks between 410 and 490 cm^{-1} belonging to the Cu-O and Zn-O vibration band supporting the XRD analysis [50,51]. The peaks of the composite samples did not show a significant difference from that of pristine ZnO, which could be due to the low content of rGO and CuO in the (rGO-ZnO)/CuO sample [52]. The FTIR spectra of GO and rGO were given in Figure S1A (see Supplementary Materials).

3.3. Morphology Characterization

The SEM image analysis provides morphological information about the samples prepared. Figure 2 shows SEM images and EDS results of ZnO, CuO-ZnO, and (rGO-ZnO)/CuO samples. The low-magnification (1 μm) SEM micrograph of the (rGO-ZnO)/CuO sample (Figure 2C) exhibited random arrays of rod-shaped morphology. The high-magnification SEM micrographs (Figure 2F) showed that the whiskers were uniformly distributed on the NRs, where some particles appear to be elongated and hexagonal. The rod-shaped crystals fall in the nanoscale regime with an average diameter of about 70 nm. Similarly, pure ZnO (Figure 2A,D) samples are composed of NRs with an average diameter of about 65 nm, whereas the image of CuO-ZnO samples (Figure 2E) illustrate the presence of one-dimensional heterostructures (ribbon-like and short rod-like nanostructures), indicating that the growth rate is slower than those in the case of ZnO NRs or (rGO-ZnO)/CuO NCs [53].

The EDS spectrum of the (rGO-ZnO)/CuO depicted in Figure 2G showed that the sample contained Zn, Cu, O, and C elements, confirming the presence of the expected elements. Furthermore, the EDS mapping analysis illustrated that the Zn, Cu, O, and C elements were homogeneously distributed throughout the (rGO-ZnO)/CuO sample. This implies that the rGO, ZnO, and CuO were properly integrated with the sample [54]. In addition, the absence of traces of other elements in the EDS spectra signifies the purity of the synthesized material and supports the XRD data [55].
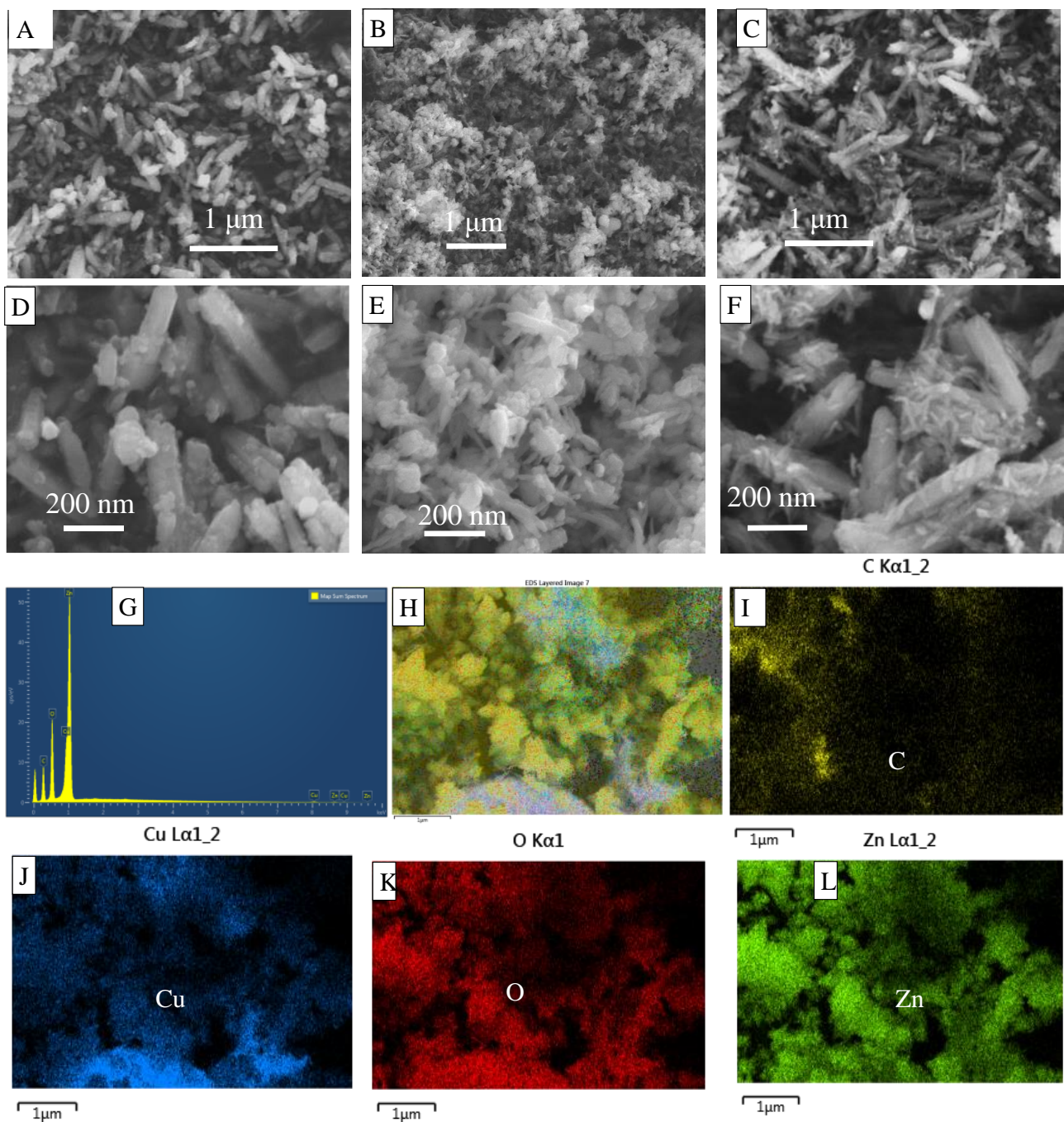
Figure 2. ZnO (**A**,**D**), CuO-ZnO, (**B**,**E**), and (rGO-ZnO)/CuO (**C**,**F**) samples with low and high magnifications; (**G**) EDS spectrum of (rGO-ZnO)/CuO; (**H**) layered image; and EDS elemental mappings of: (**I**) carbon, (**J**) copper, (**K**) oxygen, and (**L**) zinc.

A TEM image of rGO-ZO/CuO samples in Figure 3 illustrates a rod-like morphology that correlates with the SEM image. The rods consist of different sizes with lengths ranging from 230–780 nm and diameters 30–96 nm. The HRTEM image shown in Figure 3 indicates a high degree of crystallinity, as evidenced by lattice fringes [56]. Calculated inter-planar spacings were 0.190 nm, corresponding to between the hexagonal ZnO (102) and 0.187 nm between monoclinic CuO (20-2) planes. The results of this study are consistent with those found in the literature [JCPDS 361451] for ZnO and [JCPDS 481548] for CuO.
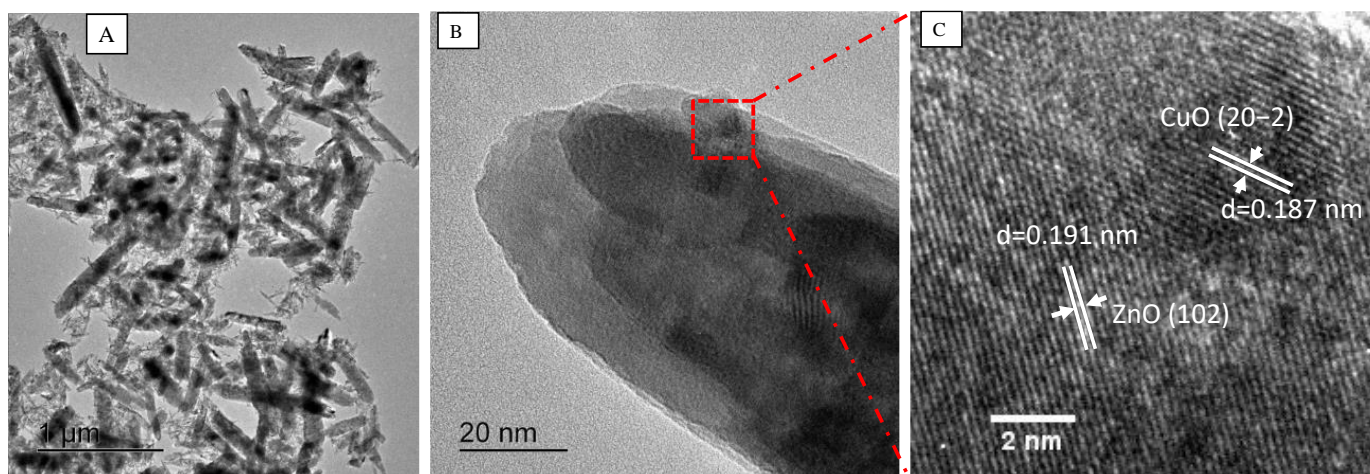
Figure 3. TEM images of (rGO-ZnO)/CuO (**A**,**B**) and HRTEM (**C**).

3.4. UV–vis and PL Analysis

The characteristic UV–vis absorption peaks of GO and rGO suspension in ethanol and photographs of their powder as well as the corresponding aqueous suspensions are given in Figure S1B–D. A strong absorbance at 235 nm and a weak shoulder at 303 nm were observed for GO. The intense band at 235 nm could be assigned to the π-π* transitions of aromatic C-C bonds, and the weaker shoulder around 303 nm could be due to the n-π* transitions of C=O bonds [57]. Upon reduction of GO, the shoulder peak at 303 nm disappeared, and that at 235 nm was red-shifted to the broader peak at around 265 nm and attributed to the aromatic C-C π→π* transition, indicating the restoration of the aromatic structure in the electronic conjugation of rGO [58]. The results for both GO and rGO are in close agreement with the values reported elsewhere [59,60]. Therefore, the shift in the 235 nm peak to the 265 nm and the color change from brown to black confirms the reduction of GO into rGO using ascorbic acid [58,61].

Similarly, the spectra displayed in Figure 4A,B belong to the absorbance and the corresponding Tauc's plot of ZnO, CuO-ZnO, and (rGO-ZnO)/CuO samples. All samples displayed a strong absorption band in the UV region ($\lambda_{max} \approx 367$ nm), which is supported by the absorbance of ZnO nanoparticles reported elsewhere [62]. As it can be seen from the Figure, both CuO-ZnO and (rGO-ZnO)/CuO samples displayed a significant portion of their absorption spectra in the visible range compared to the ZnO sample, indicating a smaller energy bandgap compared to ZnO [50]. The direct bandgap of the samples was obtained using Tauc's formula (Equation (3)) [63] from the curves fitting of $(\alpha h \nu)^2$ vs. $h \nu$, as depicted in Figure 4B [64], by extrapolating the slope of the linear region to the x-axis intersection (i.e., at $(\alpha h \nu)^2 = 0$). The estimated bandgap from the fitted graph was 3.09 eV for ZnO, 2.89 eV for CuO-ZnO, and 2.43 eV for (rGO-ZnO)/CuO samples. The result revealed that CuO-ZnO NCs possess a lower bandgap than that of ZnO NPs. Therefore, modifying ZnO with CuO and rGO resulted in improved visible light harvesting (rGO-ZnO)/CuO samples, which makes it an effective photocatalyst for pollutant dye degradation under visible light [65,66].

$$(\alpha h \nu)^n = C(h \nu - E_g) \tag{3}$$

where α, h, ν, E_g, n, and C are the absorption coefficient, Planck's constant, light frequency, bandgap energy, the power factor of the transition mode (2 for direct, 0.5 for indirect), and constant related to the material, respectively.
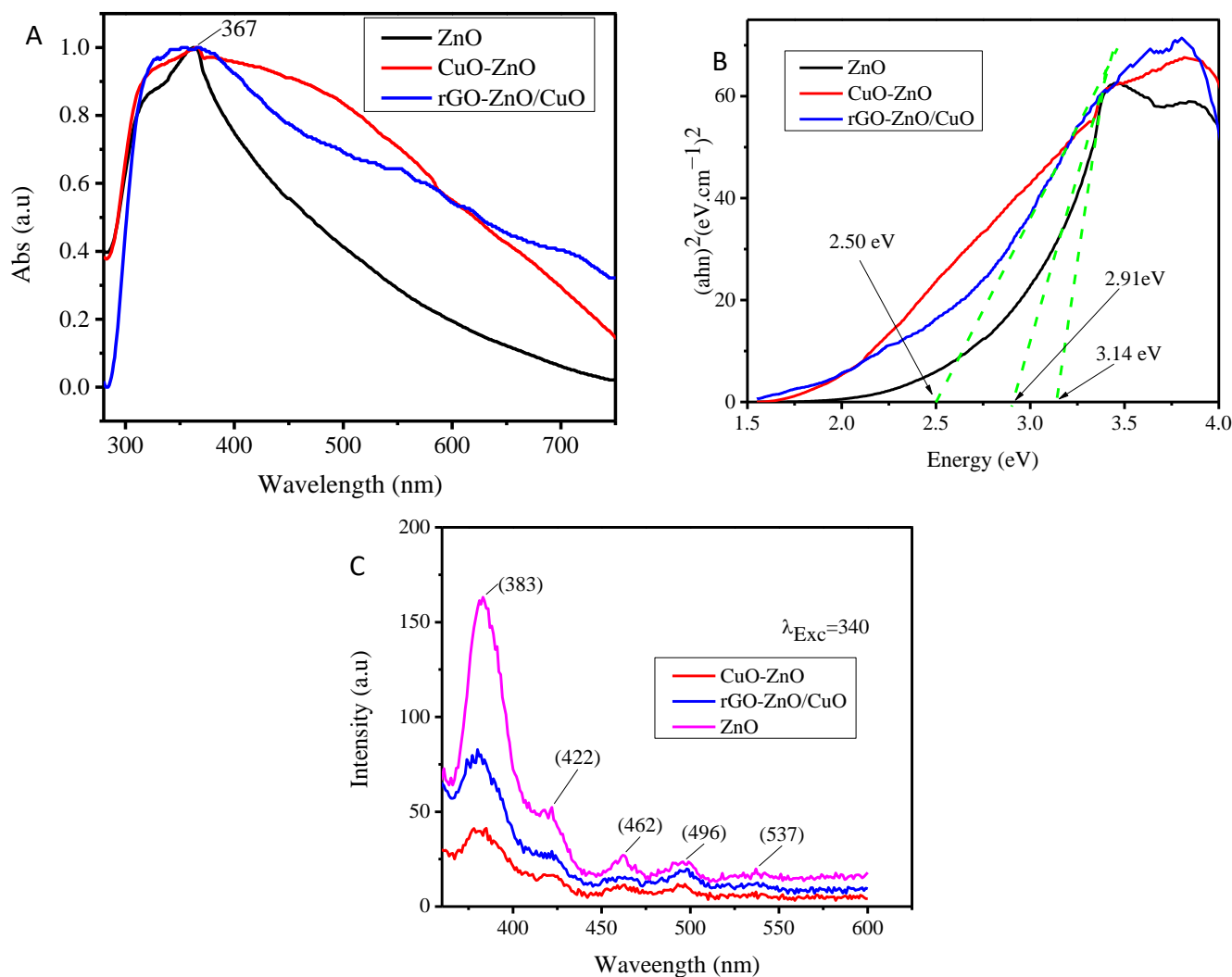
Figure 4. (**A**) UV–vis absorbance spectra, (**B**) Tauc's plot, and (**C**) PL spectra of ZnO, CuO-ZnO, and (rGO-ZnO)/CuO samples.

The room temperature emission spectra of ZnO NPs, CuO-ZnO NCs, and (rGO-ZnO)/CuO NCs are depicted in Figure 4C. At an excitation wavelength of 340 nm, the PL spectra are composed of a strong emission band at 383 nm (UV region) and relatively weaker emission bands at 462 and 496 nm (visible region), including a shoulder band at 422 nm [67]. The intense emission band at 383 nm could be assigned to e^-/h^+ recombination originating from the near band-edge of ZnO [67], whereas the other relatively weaker emission peaks in the visible range could be attributed to the recombination originating from the deep-level defects of the corresponding material [68]. As it is displayed in Figure 4C, the emission intensity from pure ZnO is higher than that of the composite both from the near band-edge and from the defect levels, indicating better e^-/h^+ separation and decreased defect level in the CuO-ZnO and (rGO-ZnO)/CuO NCs [67,69]. That is, the photogenerated electrons in the conduction band (CB) of CuO transfer effectively to the CB of ZnO and rGO sheets, preventing the direct recombination of excitons [70]. Therefore, modifying ZnO with CuO and rGO indicated that the decreased recombination rate with improved visible light absorption could make the resulting modified nanomaterials a potential candidate for photocatalysis [71].

3.5. Electrochemical Analysis

The electrochemical behavior of the synthesized photocatalyst materials was investigated by electrochemical impedance spectroscopy (EIS) and Mott–Schottky (MS) analysis. In this study, the EIS and MS results of the (rGO-ZnO)/CuO NCs were compared to those of CuO-ZnO and ZnO. An EIS survey of the resistance and capacitance properties of synthesized nanomaterials across the semiconductor-electrolyte interface was carried out to examine charge carriers' separation, transfer, and recombination behavior. According to the impedance analysis shown in Figure S2A, CuO-ZnO NCs displayed the smallest impedance arc radius compared to ZnO NRs and (rGO-ZnO)/CuO NCs, indicating a suppressed recombination rate due to fast electron transfer across the interface [72]. In the EIS analysis, Nyquist plots with a smaller semicircle arc indicate materials with better conductivity leading to facilitated transfer of charge carriers, which could lead to enhanced photocatalytic performance [73]. The results obtained from the EIS are consistent with the PL analysis (Figure 4C).

Similarly, the Mott–Schottky plots of (rGO-ZnO)/CuO NCs, CuO-ZnO NCs, and ZnO NRs are illustrated in Figure S2B–D. A plot of ZnO NRs showed a positive slope, indicating an n-type semiconductor with a flat band potential (E_{fb}) of −0.4 V vs. Ag/AgCl. However, in the case of (rGO-ZnO)/CuO NCs and CuO-ZnO NCs, the co-existence of negative and positive slopes was observed, confirming the effective development of p-n heterojunction between CuO and ZnO [74]. The values were shown in Figure S2C,D with −0.4 and 1.2 V for CuO-ZnO NCs and 0.37 and 1.3 V for (rGO-ZnO)/CuO NCs vs. Ag/AgCl. The potentials relative to the reversible hydrogen electrode (RHE) were obtained using the Nernst equation and potentials measured vs. Ag/AgCl (Equation (4)) [75].

$$E_{RHE} = E_{Ag/AgCl} + E^0_{Ag/AgCl} + 0.059 \text{ pH} \tag{4}$$

where $E^0_{Ag/AgCl(sat)}$ = 0.197 V, and the electrolyte pH is 7.

Hence, the corresponding E_{fb} relative to RHE is given in Table S1. According to the literature, the E_{fb} of the n-type semiconductors is close to the conduction band-edge (i.e., CB is more negative E_{fb} by ~0.1 V), and that of the p-type semiconductors is close to the valence band-edge (i.e., VB is more positive than E_{fb} by ~0.1 V) [76]. Combining these values with the bandgap energy obtained from Tauc's formula, the VB of ZnO and the CB of CuO can be calculated using Equation (5) [76]. Thus, using the E_{fb} and the calculated band gaps, the conduction and valence band potentials of ZnO NRs, CuO-ZnO NCs, and (rGO-ZnO)/CuO NCs were determined (Table S1). In the (rGO-ZnO)/CuO NCs, the CB and VB potentials of ZnO and CuO were found to be 0.14 and 2.57 V for ZnO and −0.42 and 2.01 V for CuO, respectively. Further, from the band-edge position of VB and CB of ZnO and CuO in the (rGO-ZnO)/CuO NCs, type II staggered band alignment was formed between ZnO and CuO.

$$E_{VB} = E_{CB} + E_g \tag{5}$$

3.6. Photocatalytic Activity and Mechanism

The photocatalytic performance of ZnO NRs, CuO-ZnO NCs, and (rGO-ZnO)/CuO NCs were evaluated against MB degradation as a test organic pollutant under visible light irradiation (Figure 5). The aqueous solution of MB showed a strong absorbance peak at 664 nm [77]. The absorbance of MB solution in the presence of catalysts showed a gradual decrease under irradiation indicating MB degradation. According to the result, pure ZnO NRs degraded about 37% of the initial MB concentration within 105 min, whereas CuO-ZnO NCs and (rGO-ZnO)/CuO NCs degraded about 80% and 90% of the initial MB within 105 min, respectively (Figure 5A,D). In addition, the kinetics of the degradation reaction was displayed in Figure 5E,F. According to the linear fit of $\ln(C_t/C_o)$ vs. time (Figure 5F), the rate constant (k) was found to be 0.0045 min^{-1}, 0.0158 min^{-1}, and 0.0221 min^{-1} for ZnO, CuO-ZnO NCs, and (rGO-ZnO)/CuO NCs, respectively. This enhancement in the photocatalytic performance compared to pure ZnO NRs signifies that the introduction of

CuO and rGO improved the visible light absorption and suppressed the rate of recombination [15]. The result from the optical studies supported the improved performance of the NCs. Particularly, the weaker PL intensity of the composite than of pure ZnO suggests the enhanced separation of the excitons [78,79]. In other words, a higher charge separation assists the migration of excitons to the surface and reacts with the adsorbed species, leading to the higher activities of the composite compared to the pristine ZnO [79]. The ratio constant (rate constant per g of catalyst) of (rGO-ZnO)/CuO NCs for the photocatalytic degradation of MB compared to the previously reported materials is given in Table 1. It indicates that (rGO-ZnO)/CuO NCs showed remarkable performance.
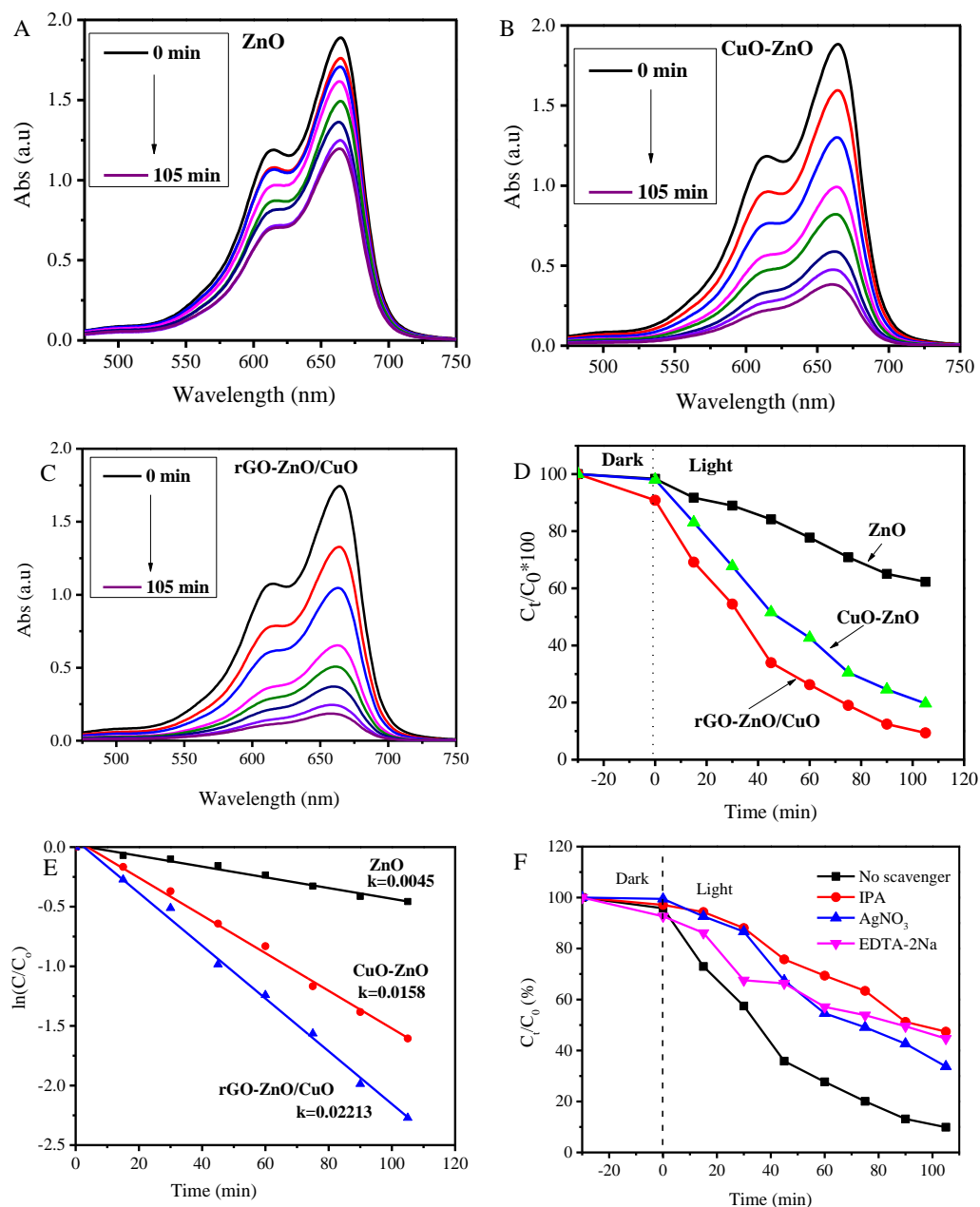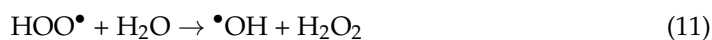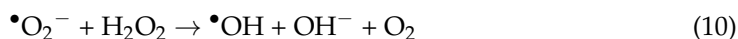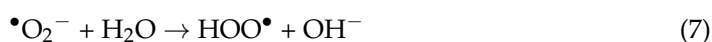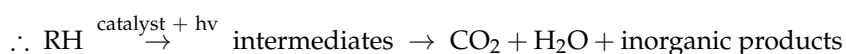

Figure 5. Progress of MB degradation using catalysts: ZnO NRs (**A**), CuO-ZnO NCs (**B**), and (rGO-ZnO)/CuO NCs (**C**); (**D**) plots of C_t/C_0 vs. t; (**E**) plots of $\ln(C_t/C_0)$ vs. t for MB degradation using ZnO, CuO-ZnO, and (rGO-ZnO)/CuO NCs; (**F**) effect of scavengers on the photocatalytic degradation of MB using (rGO-ZnO)/CuO NCs.

Table 1. Comparison of (rGO-ZnO)/CuO NCs to previous reports against photocatalytic degradation of MB.

Catalyst	Synthesis Method	Experimental Conditions			Performance		Ref.
		Catalyst (mg)	Conc. of MB	Light	Efficiency (%)	Ratio Constant, K (min^{-1}g^{-1})	
ZnO/CuO	Combustion	40	20 ppm	Solar	93 in 60 min	0.5575	[51]
CuO-ZnO	Wet chemical	5	5 μM	Solar	93.8 in 20 min	27.2	[18]
ZnO–CuO	Co-precipitation	25	0.001 M	Vis	95.6	0.94	[16]
GO–CuFe$_2$O$_4$–ZnO	Combustion	10	40 ppm	Solar	100 in 40 min	9.94	[55]
ZnO/CuO	Biocombustion	40	10 ppm	UV	99.2 in 60 min	1.45	[77]
MoS$_2$-ZnO-rGO	Hydrothermal	100	20 ppm	Solar	90 in 75 min	-	[48]
(rGO-ZnO)/CuO	MW	40	10 ppm	Vis	90 in 105 min	11.7	This work

A trapping experiment was performed to find out the main active species involved in photocatalysis using ethylenediaminetetraacetic acid disodium (EDTA-2Na), AgNO$_3$, and isopropanol (IPA) to scavenge photogenerated holes (h$^+$), superoxide radicals ($^\bullet$O$_2^-$), and hydroxyl radicals ($^\bullet$OH), respectively [79]. The results of the experiment are illustrated in Figure 5F. As can be seen from the Figure, the addition of the scavengers resulted in decreased efficiency of MB photocatalytic degradation, indicating that h$^+$, $^\bullet$OH, and $^\bullet$O$_2^-$ are the active species involved. These active species could be generated in varieties of ways. Under visible light illumination of (rGO-ZnO)/CuO, excitons generate where e$^-$ resides in the CB, and h$^+$ resides in the VB, leading to the generation of other active species (i.e., reactive oxygen species): (i) The $^\bullet$O$_2^-$ could be generated by the reaction between photogenerated electrons and adsorbed oxygen, where CB potentials are more negative than the potential of O$_2$/$^\bullet$O$_2^-$ (-0.16V) (Equation (6)) [80]. The $^\bullet$O$_2^-$ further reacts and forms other reactive oxygen species (Equations (7), (8) and (10)). (ii) The $^\bullet$OH could be generated as shown in the Equations (Equations (10)–(13)). The $^\bullet$OH degrades MB to yield degraded products (Equations (15) and (16)). (iii) The photogenerated holes in the VB or trap states react with the adsorbed species (OH$^-$, H$_2$O, or MB) and generate reactive radicals that further react with other species and degrade the pollutants (Equations (12)–(14) and (16)). Oxidation of the adsorbed species (H$_2$O, OH$^-$) to generate $^\bullet$OH occurs when the VB edge potentials are more positive than that of OH$^-$/$^\bullet$OH (1.9V vs. NHE) and H$_2$O/$^\bullet$OH + H$^+$ (2.73 V vs. NHE) [81].

$$O_2 + e^- \rightarrow {}^\bullet O_2^- \tag{6}$$

$$^\bullet O_2^- + H_2O \rightarrow HOO^\bullet + OH^- \tag{7}$$

$$^\bullet O_2^- + H^+ \rightarrow HOO^\bullet \tag{8}$$

$$HOO^\bullet + H^+ + e^- \rightarrow H_2O_2 \tag{9}$$

$$^\bullet O_2^- + H_2O_2 \rightarrow {}^\bullet OH + OH^- + O_2 \tag{10}$$

$$HOO^\bullet + H_2O \rightarrow {}^\bullet OH + H_2O_2 \tag{11}$$

$$H_2O + h^+ \rightarrow {}^\bullet OH + H^+ \tag{12}$$

$$OH^- + h^+ \rightarrow {}^\bullet OH \tag{13}$$

$$RH + h^+ \rightarrow R^\bullet + H^+ \tag{14}$$

$$RH + {}^{\bullet}OH \rightarrow R^{\bullet} + H_2O \tag{15}$$

$$R^{\bullet} \rightarrow \text{intermediate/final degraded product} \tag{16}$$

$$\therefore RH \xrightarrow{\text{catalyst} + h\nu} \text{intermediates} \rightarrow CO_2 + H_2O + \text{inorganic products}$$

where RH stands for MB dye.

3.7. Catalytic Reduction Activity

Catalytic reduction of 4-NP to 4-aminophenol (4-AP) was used to evaluate the performance of the prepared (rGO-ZnO)/CuO in the presence of $NaBH_4$. Figure 6 shows the reduction progress and kinetics of the (rGO-ZnO)/CuO NCs. The absorbance of the 4-NP aqueous solution showed maximum absorbance at 319 nm. However, the addition of $NaBH_4$ made the band at 319 nm disappear, and a new band emerged at 405 nm, indicating the formation of a 4-nitrophenolate ion (Figure 6A). Upon addition of catalysts to the $NaBH_4$ containing 4-NP solution, absorbance at 405 was decreased, while a new band at 300 nm appeared, revealing the formation of 4-AP. Both (rGO-ZnO)/CuO and CuO-ZnO NCs reduced almost all 4-NP in less than 9 min, whereas ZnO NRs exhibited insignificant catalytic activity, showing that ZnO has lower catalytic efficiency compared to CuO-ZnO and (rGO-ZnO)/CuO NCs (Figure 6B–D).

The kinetics analysis of the reduction reaction of 4-NP using $NaBH_4$ in the presence of ZnO NRs, CuO-ZnO NCs, and (rGO-ZnO)/CuO NCs is given in Figure 6E,F. Based on the kinetic analysis, it was found that the data most closely fitted the pseudo-first-order reaction equation (Equation (2)) [82]. The rate constants of ZnO NRs, CuO-ZnO NCs, and (rGO-ZnO)/CuO NCs were found to be 0.00026, 0.465, and 0.468 min^{-1}, respectively. The result indicated that the rate of reduction reaction was high when the nanocomposites were used (Figure 6F). The mechanism of the 4-NP reduction reaction involves the following: (i) adsorption of BH_4^- and 4-NP to the catalyst surface, (ii) transfer of electrons from BH_4^- to the adsorbed 4-NP [83], (iii) transfer of protons from the BH_4^- and H_2O to the 4-NP [84], and (iv) desorption steps. In the (rGO-ZnO)/CuO NCs, the highest rate of reaction could be related to the presence of rGO and the CuO-ZnO p-n heterojunction facilitating the adsorption and transfer of charged species [43]. The key steps in 4-NP reduction by (rGO-ZnO)/CuO NCs are illustrated in Scheme 2.
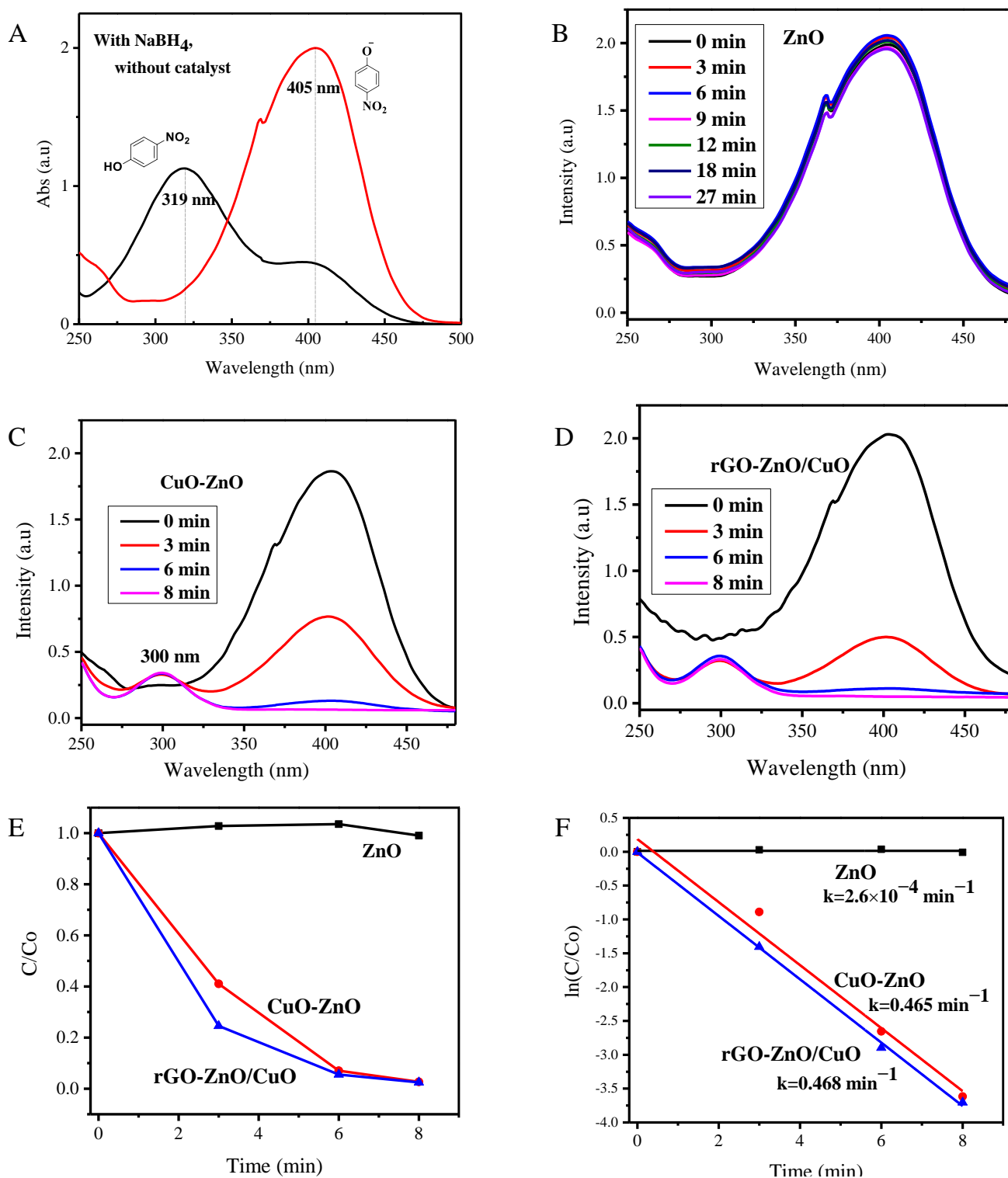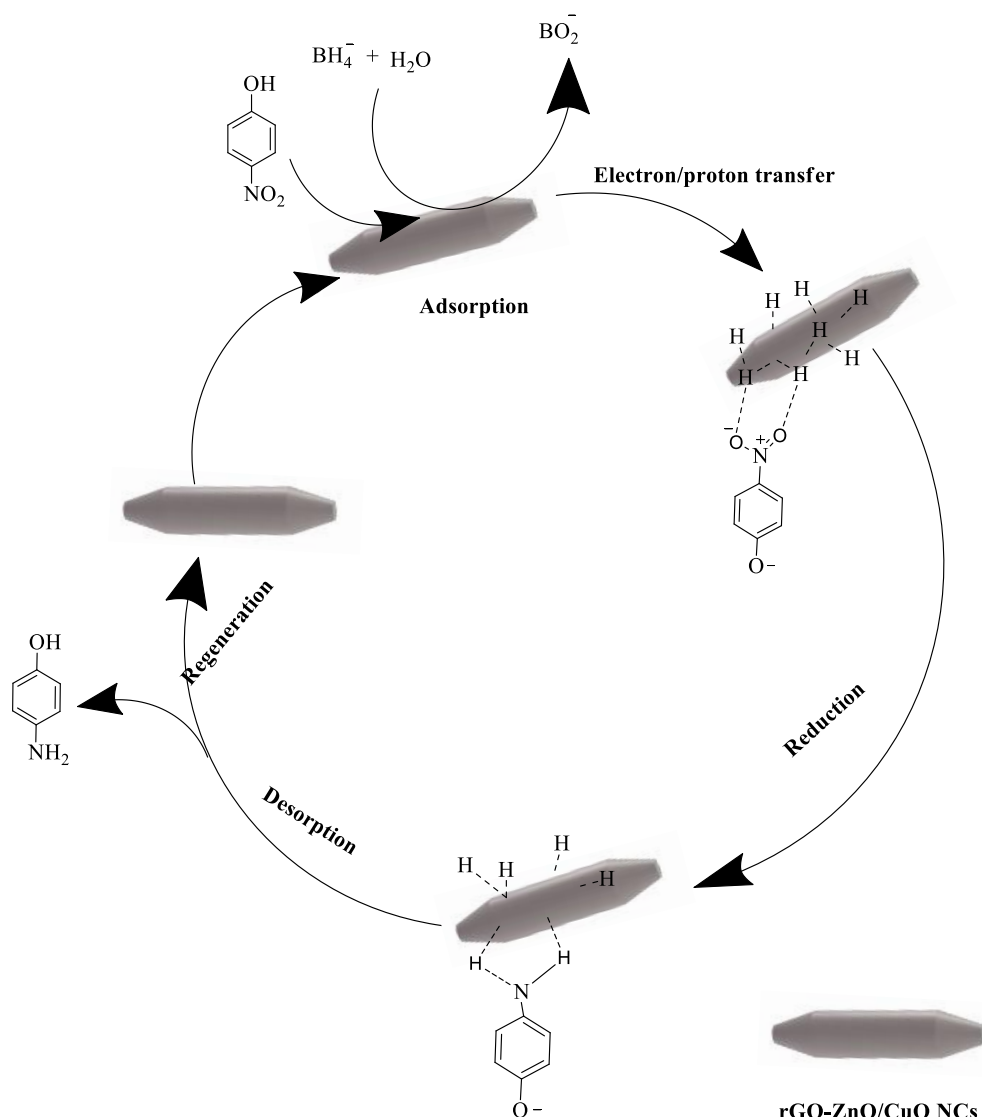
Figure 6. Photocatalytic degradation of MB using catalysts: ZnO NRs (**A**), CuO-ZnO NCs (**B**), and (rGO-ZnO)/CuO NCs (**C**); (**D**) plots of C_t/C_0 vs. reaction time (min); (**E**) plots of $\ln(C_t/C_0)$ vs. reaction time (min) for MB degradation using ZnO, CuO-ZnO, and (rGO-ZnO)/CuO NCs; (**F**) effect of scavengers on the photocatalytic degradation of MB using (rGO-ZnO)/CuO NCs.

Scheme 2. Mechanism of 4-NP reduction in the presence of (rGO-ZnO)/CuO NCs and NaBH$_4$.

4. Conclusions

In summary, rod-shaped (rGO-ZnO)/CuO NCs were successfully synthesized via a simple and repeatable MW-assisted method. The synthesized samples were characterized using XRD, spectroscopic, and microscopic techniques. The crystalline structure of (rGO-ZnO)/CuO NCs with CuO and ZnO phases was obtained. Moreover, EDS results confirmed that the sample was composed of O, C, Cu, and Zn elements distributed homogeneously. Additionally, (rGO-ZnO)/CuO NCs exhibited enhanced visible light absorption with a reduced e$^-$/h$^+$ recombination rate compared to the pristine ZnO NPs. Furthermore, (rGO-ZnO)/CuO NCs showed enhanced performance against MB degradation with rate constants of 0.02213 min^{-1} and that of 4-NP reduction with 0.468 min^{-1}. This makes (rGO-ZnO)/CuO NCs a potential candidate for treating water polluted by organic dyes.

References

1. Khalid, Z.B.; Nasrullah, M.; Nayeem, A.; Wahid, Z.; Singh, L.; Krishnan, S. Application of 2D Graphene-Based Nanomaterials for Pollutant Removal from Advanced Water and Wastewater Treatment Processes. In *ACS Symposium Series*; American Chemical Society: New York, NY, USA, 2020; pp. 191–217.

2. Lu, F.; Astruc, D. Nanomaterials for removal of toxic elements from water. *Coord. Chem. Rev.* **2018**, *356*, 147–164. [CrossRef]

3. Ibrahim, R.; Hayyan, M.; AlSaadi, M.; Hayyan, A.; Ibrahim, S. Environmental application of nanotechnology: Air, soil, and water. *Environ. Sci. Pollut. Res.* **2016**, *23*, 13754–13788. [CrossRef]

4. Zhang, Y.; Wu, B.; Xu, H.; Liu, H.; Wang, M.; He, Y.; Pan, B. Nanomaterials-enabled water and wastewater treatment. *NanoImpact* **2016**, *3*, 22–39. [CrossRef]

5. Silva, C.; Faria, J. Effect of key operational parameters on the photocatalytic oxidation of phenol by nanocrystalline sol-gel TiO$_2$ under UV irradiation. *J. Mol. Catal. A Chem.* **2009**, *305*, 147–154. [CrossRef]

6. Mandeep; Gupta, G.; Liu, H.; Shukla, P. Pulp and paper industry–based pollutants, their health hazards and environmental risks. *Curr. Opin. Environ. Sci. Health* **2019**, *12*, 48–56. [CrossRef]

7. Sivaram, N.; Gopal, P.; Barik, D. Toxic waste from textile industries. In *Energy from Toxic Organic Waste for Heat and Power Generation*; Elsevier: Amsterdam, The Netherlands, 2018; pp. 43–54.

8. Ahmad, M.; Mushtaq, S.; Al Qahtani, H.; Sedky, A.; Alam, M. Investigation of TiO$_2$ Nanoparticles Synthesized by Sol-Gel Method for Effectual Photodegradation, Oxidation and Reduction Reaction. *Crystals* **2021**, *11*, 1456. [CrossRef]

9. Alam, M.; Al Qahtani, H.; Aamir, M.; Abuzir, A.; Khan, M.; Albuhulayqah, M.; Mushtaq, S.; Zaidi, N.; Ramya, A. Phyto Synthesis of Manganese-Doped Zinc Nanoparticles Using Carica papaya Leaves: Structural Properties and Its Evaluation for Catalytic, Antibacterial and Antioxidant Activities. *Polymers* **2022**, *14*, 1827. [CrossRef]

10. Anwer, H.; Mahmood, A.; Lee, J.; Kim, K.; Park, J.; Yip, A. Photocatalysts for degradation of dyes in industrial effluents: Opportunities and challenges. *Nano Res.* **2019**, *12*, 955–972. [CrossRef]

11. Gadipelly, C.; Mannepalli, L. Nano-metal oxides for organic transformations. *Curr. Opin. Green Sustain. Chem.* **2019**, *15*, 20–26. [CrossRef]

12. Das, T.; Remanan, S.; Ghosh, S.; Das, N. An environment friendly free-standing cellulose membrane derived for catalytic reduction of 4-nitrophenol: A sustainable approach. *J. Environ. Chem. Eng.* **2021**, *9*, 104596. [CrossRef]

13. Das, T.; Das, N. Advances on catalytic reduction of 4-nitrophenol by nanostructured materials as benchmark reaction. *Int. Nano Lett.* **2022**, *12*, 223–242. [CrossRef]

14. Nagajyothi, P.; Vattikuti, S.V.P.; Devarayapalli, K.; Yoo, K.; Shim, J.; Sreekanth, T. Green synthesis: Photocatalytic degradation of textile dyes using metal and metal oxide nanoparticles-latest trends and advancements. *Crit. Rev. Environ. Sci. Technol.* **2020**, *50*, 2617–2723. [CrossRef]

15. Pirhashemi, M.; Habibi-Yangjeh, A.; Pouran, S.R. Review on the criteria anticipated for the fabrication of highly efficient ZnO-based visible-light-driven photocatalysts. *J. Ind. Eng. Chem.* **2018**, *62*, 1–25. [CrossRef]

16. Ullah, H.; Mushtaq, L.; Ullah, Z.; Fazal, A.; Khan, A. Effect of vegetable waste extract on microstructure, morphology, and photocatalytic efficiency of ZnO–CuO nanocomposites. *Inorg. Nano-Metal Chem.* **2021**, *51*, 963–975. [CrossRef]

17. Ong, C.; Ng, L.; Mohammad, A. A review of ZnO nanoparticles as solar photocatalysts: Synthesis, mechanisms and applications. *Renew. Sustain. Energy Rev.* **2018**, *81*, 536–551. [CrossRef]

18. Sahu, K.; Bisht, A.; Kuriakose, S.; Mohapatra, S. Two-dimensional CuO-ZnO nanohybrids with enhanced photocatalytic performance for removal of pollutants. *J. Phys. Chem. Solids* **2020**, *137*, 109223. [CrossRef]

19. Liu, C.; Meng, F.; Zhang, L.; Zhang, D.; Wei, S.; Qi, K.; Fan, J.; Zhang, H.; Cui, X. CuO/ZnO heterojunction nanoarrays for enhanced photoelectrochemical water oxidation. *Appl. Surf. Sci.* **2019**, *469*, 276–282. [CrossRef]

20. Taraka, T.Y.; Gautam, A.; Jain, S.; Bojja, S.; Pal, U. Controlled addition of Cu/Zn in hierarchical CuO/ZnO p-n heterojunction photocatalyst for high photoreduction of CO_2 to MeOH. *J. CO2 Util.* **2019**, *31*, 207–214. [CrossRef]

21. Kumaresan, N.; Sinthiya, M.; Ramamurthi, K.; Babu, R.R.; Sethuraman, K. Visible light driven photocatalytic activity of ZnO/CuO nanocomposites coupled with rGO heterostructures synthesized by solid-state method for RhB dye degradation. *Arab. J. Chem.* **2020**, *13*, 3910–3928. [CrossRef]

22. Li, X.; Shen, R.; Ma, S.; Chen, X.; Xie, J. Graphene-based heterojunction photocatalysts. *Appl. Surf. Sci.* **2018**, *430*, 53–107. [CrossRef]

23. Liu, F.; Che, Y.; Chai, Q.; Zhao, M.; Lv, Y.; Sun, H.; Wang, Y.; Sun, J.; Zhao, C. Construction of rGO wrapping Cu_2O/ZnO heterostructure photocatalyst for PNP and PAM degradation. *Environ. Sci. Pollut. Res.* **2019**, *26*, 25286–25300. [CrossRef] [PubMed]

24. Zhen, Z.; Zhu, H. Structure and properties of graphene. In *Graphene: Fabrication, Characterizations, Properties and Applications*; Elsevier: Amsterdam, The Netherlands, 2017; pp. 1–12.

25. Zhang, G.; Sun, S. *Advantages and Challenges of One-Dimensional Nanostructures for Fuel Cell Applications*; Elsevier Ltd.: Amsterdam, The Netherlands, 2017.

26. Ramos, P.; Sánchez, L.; Rodriguez, J. A review on improving the efficiency of photocatalytic water decontamination using ZnO nanorods. *J. Sol-Gel Sci. Technol.* **2022**, *102*, 105–124. [CrossRef]

27. Zhou, W.; Zhang, X.; Zhao, D.; Gao, M.; Xie, S. ZnO nanorods: Morphology control, optical properties, and nanodevice applications. *Sci. China Phys. Mech. Astron.* **2013**, *56*, 2243–2265. [CrossRef]

28. Aspoukeh, P.; Barzinjy, A.; Hamad, S. Synthesis, properties and uses of ZnO nanorods: A mini review. *Int. Nano Lett.* **2022**, *12*, 153–168. [CrossRef]

29. Liu, T.; Wang, Q.; Jiang, P. Morphology-dependent photo-catalysis of bare zinc oxide nanocrystals. *RSC Adv.* **2013**, *3*, 12662–12670. [CrossRef]

30. Man, H.; Wen, C.; Luo, W.; Bian, J.; Wang, W.; Li, C. Simultaneous deSOx and deNOx of marine vessels flue gas on ZnO-CuO/rGO: Photocatalytic oxidation kinetics. *J. Ind. Eng. Chem.* **2020**, *92*, 77–87. [CrossRef]

31. Tantubay, K.; Das, P.; Sen, M.B. Ternary reduced graphene oxide–CuO/ZnO nanocomposite as a recyclable catalyst with enhanced reducing capability. *J. Environ. Chem. Eng.* **2020**, *8*, 103818. [CrossRef]

32. Firoozi, S.; Hosseini-Sarvari, M. Visible-Light-Induced C-P-Bond Formation Using Reduced Graphene Oxide Decorated with Copper Oxide/Zinc Oxide (rGO/CuO/ZnO) as Ternary Recyclable Nanophotocatalyst. *ChemistrySelect* **2021**, *6*, 1764–1771. [CrossRef]

33. Maity, C.; Hatui, G.; Verma, K.; Udayabhanu, G.; Pathak, D.; Nayak, G. Single pot fabrication of N doped reduced GO (N-rGO) /ZnO-CuO nanocomposite as an efficient electrode material for supercapacitor application. *Vacuum* **2018**, *157*, 145–154. [CrossRef]

34. Wang, C.; Zhu, J.; Liang, S.; Bi, H.; Han, Q.; Liu, X.; Wang, X. Reduced graphene oxide decorated with CuO-ZnO hetero-junctions: Towards high selective gas-sensing property to acetone. *J. Mater. Chem. A* **2014**, *2*, 18635–18643. [CrossRef]

35. Jyoti; Varma, G.D. Synthesis of CuO-ZnO/rGO ternary composites for superior NO_2 gas sensor at room temperature. *Mater. Res. Express* **2019**, *6*, 035011. [CrossRef]

36. Jyoti; Srivastava, A.; Varma, G. Highly selective and efficient room temperature NO_2 gas sensors based on Zn-doped CuO nanostructure-rGO hybrid. *J. Mater. Sci. Mater. Electron.* **2018**, *29*, 10640–10655. [CrossRef]

37. Asgar, H.; Deen, K.; Haider, W. Estimation of electrochemical charge storage capability of ZnO/CuO/reduced graphene oxide nanocomposites. *Int. J. Energy Res.* **2020**, *44*, 1580–1593. [CrossRef]

38. Schütz, M.; Xiao, L.; Lehnen, T.; Fischer, T.; Mathur, S. Microwave-assisted synthesis of nanocrystalline binary and ternary metal oxides. *Int. Mater. Rev.* **2018**, *63*, 341–374. [CrossRef]

39. Kumar, A.; Kuang, Y.; Liang, Z.; Sun, X. Microwave chemistry, recent advancements, and eco-friendly microwave-assisted synthesis of nanoarchitectures and their applications: A review. *Mater. Today Nano* **2020**, *11*, 100076. [CrossRef]

40. Zaaba, N.; Foo, K.; Hashim, U.; Tan, S.; Liu, W.; Voon, C. Synthesis of Graphene Oxide using Modified Hummers Method: Solvent Influence. *Procedia Eng.* **2017**, *184*, 469–477. [CrossRef]

41. De Silva, K.; Huang, H.; Yoshimura, M. Progress of reduction of graphene oxide by ascorbic acid. *Appl. Surf. Sci.* **2018**, *447*, 338–346. [CrossRef]

42. Prakash, A.; Sahu, N.; Bahadur, D. Enhanced photocatalytic performance of ZnO-reduced graphene oxide hybrid synthesized via ultrasonic probe-assisted study. In *AIP Conference Proceedings*; American Institute of Physics: College Park, MD, USA, 2013; Volume 1512, pp. 312–313.

43. Zelekew, O.; Kuo, D. Facile synthesis of SiO$_2$@CuxO@TiO$_2$ heterostructures for catalytic reductions of 4-nitrophenol and 2-nitroaniline organic pollutants. *Appl. Surf. Sci.* **2017**, *393*, 110–118. [CrossRef]

44. Bolaghi, Z.K.; Masoudpanah, S.; Hasheminiasari, M. Photocatalytic activity of ZnO/RGO composite synthesized by one-pot solution combustion method. *Mater. Res. Bull.* **2019**, *115*, 191–195. [CrossRef]

45. Alam, S.; Sharma, N.; Kumar, L. Synthesis of Graphene Oxide (GO) by Modified Hummers Method and Its Thermal Reduction to Obtain Reduced Graphene Oxide (rGO)*. *Graphene* **2017**, *6*, 1–18. [CrossRef]

46. Thakur, S.; Karak, N. Green reduction of graphene oxide by aqueous phytoextracts. *Carbon N. Y.* **2012**, *50*, 5331–5339. [CrossRef]

47. Omar, F.; Ming, H.N.; Hafiz, S.; Ngee, L. Microwave synthesis of zinc oxide/reduced graphene oxide hybrid for adsorption-photocatalysis application. *Int. J. Photoenergy* **2014**, *2014*, 176835. [CrossRef]

48. Priyadharsan, A.; Shanavas, S.; Vasanthakumar, V.; Balamuralikrishnan, B.; Anbarasan, P. Synthesis and investigation on synergetic effect of rGO-ZnO decorated MoS$_2$ microflowers with enhanced photocatalytic and antibacterial activity. *Colloids Surf. A Physicochem. Eng. Asp.* **2018**, *559*, 43–53.

49. Harish, S.; Archana, J.; Sabarinathan, M.; Navaneethan, M.; Nisha, K.; Ponnusamy, S.; Muthamizhchelvan, C.; Ikeda, H.; Aswal, D.K.; Hayakawa, Y. Controlled structural and compositional characteristic of visible light active ZnO/CuO photocatalyst for the degradation of organic pollutant. *Appl. Surf. Sci.* **2017**, *418*, 103–112. [CrossRef]

50. Islam, M.; Dominguez, A.; Alvarado-Tenorio, B.; Bernal, R.; Montes, M.; Noveron, J. Sucrose-Mediated Fast Synthesis of Zinc Oxide Nanoparticles for the Photocatalytic Degradation of Organic Pollutants in Water. *ACS Omega* **2019**, *4*, 6560–6572. [CrossRef]

51. Renuka, L.; Anantharaju, K.; Vidya, Y.; Nagaswarupa, H.; Prashantha, S.; Nagabhushana, H. Synthesis of Sunlight Driven ZnO/CuO Nanocomposite: Characterization, Optical, Electrochemical and Photocatalytic Studies. *Mater. Today Proc.* **2017**, *4*, 11782–11790. [CrossRef]

52. Govindasamy, G.; Mydin, R.; Sreekantan, S.; Harun, N. Compositions and antimicrobial properties of binary ZnO–CuO nanocomposites encapsulated calcium and carbon from Calotropis gigantea targeted for skin pathogens. *Sci. Rep.* **2021**, *11*, 99. [CrossRef]

53. Parra, M.; Haque, F. Poly (Ethylene Glycol) (PEG)-assisted shape-controlled synthesis of one-dimensional ZnO nanorods. *Optik* **2015**, *126*, 1562–1566. [CrossRef]

54. Wang, Y.; Jiang, F.; Chen, J.; Sun, X.; Xian, T.; Yang, H. In Situ Construction of CNT/CuS Hybrids and Their Application in Photodegradation for Removing Organic Dyes. *Nanomaterials* **2020**, *10*, 178. [CrossRef]

55. Kumar, A.; Rout, L.; Achary, L.; Mohanty, S.; Dash, P. A combustion synthesis route for magnetically separable graphene oxide-CuFe2O4-ZnO nanocomposites with enhanced solar light-mediated photocatalytic activity. *New J. Chem.* **2017**, *41*, 10568–10583. [CrossRef]

56. Galani, S.; Panda, A. Enhanced Thermocatalytic Activity of Porous Yellow ZnO Nanoflakes: Defect- and Morphology-Induced Perspectives. *Chem.—An Asian J.* **2019**, *14*, 612–620. [CrossRef]

57. Arias, F.; Guevara, M.; Tene, T.; Angamarca, P.; Molina, R.; Valarezo, A.; Salguero, O.; Vacacela Gomez, C.; Arias, M.; Caputi, L.S. The adsorption of methylene blue on eco-friendly reduced graphene oxide. *Nanomaterials* **2020**, *10*, 4–5. [CrossRef] [PubMed]

58. Mahendran, G.; Ramalingam, S.; Rayappan, J.; Kesavan, S.; Periathambi, T.; Nesakumar, N. Green preparation of reduced graphene oxide by Bougainvillea glabra flower extract and sensing application. *J. Mater. Sci. Mater. Electron.* **2020**, *31*, 14345–14356. [CrossRef]

59. Johra, F.; Lee, J.; Jung, W. Facile and safe graphene preparation on solution based platform. *J. Ind. Eng. Chem.* **2014**, *20*, 2883–2887. [CrossRef]

60. Momeni, M.; Ghayeb, Y.; Menati, M. Fabrication, characterization and photoelectrochemical properties of cuprous oxide-reduced graphene oxide photocatalysts for hydrogen generation. *J. Mater. Sci. Mater. Electron.* **2018**, *29*, 4136–4146. [CrossRef]

61. Rabchinskii, M.; Dideikin, A.; Kirilenko, D.; Baidakova, M.V.; Shnitov, V.V.; Roth, F.; Konyakhin, S.V.; Besedina, N.A.; Pavlov, S.I.; Kuricyn, R.A.; et al. Facile reduction of graphene oxide suspensions and films using glass wafers. *Sci. Rep.* **2018**, *8*, 14154. [CrossRef]

62. Singh, D.; Pandey, D.; Yadav, R.; Singh, D. A study of ZnO nanoparticles and ZnO-EG nanofluid. *J. Exp. Nanosci.* **2013**, *8*, 731–741. [CrossRef]

63. Saravanakkumar, D.; Sivaranjani, S.; Kaviyarasu, K.; Ayeshamariam, A.; Ravikumar, B.; Pandiarajan, S.; Veeralakshmi, C.; Jayachandran, M.; Maaza, M. Synthesis and characterization of ZnO-CuO nanocomposites powder by modified perfume spray pyrolysis method and its antimicrobial investigation. *J. Semicond.* **2018**, *39*, 033001. [CrossRef]

64. Lei, X.; Cao, Y.; Chen, Q.; Ao, X.; Fang, Y.; Liu, B. ZIF-8 derived hollow CuO/ZnO material for study of enhanced photocatalytic performance. *Colloids Surf. A Physicochem. Eng. Asp.* **2019**, *568*, 1–10. [CrossRef]

65. Sathishkumar, P.; Sweena, R.; Wu, J.; Anandan, S. Synthesis of CuO-ZnO nanophotocatalyst for visible light assisted degradation of a textile dye in aqueous solution. *Chem. Eng. J.* **2011**, *171*, 136–140. [CrossRef]

66. Yu, J.; Zhuang, S.; Xu, X.; Zhu, W.; Feng, B.; Hu, J. Photogenerated electron reservoir in hetero-p-n CuO-ZnO nanocomposite device for visible-light-driven photocatalytic reduction of aqueous Cr(vi). *J. Mater. Chem. A* **2015**, *3*, 1199–1207. [CrossRef]

67. Xu, L.; Zhou, Y.; Wu, Z.; Zheng, G.; He, J.; Zhou, Y. Improved photocatalytic activity of nanocrystalline ZnO by coupling with CuO. *J. Phys. Chem. Solids* **2017**, *106*, 29–36. [CrossRef]

68. Lavín, A.; Sivasamy, R.; Mosquera, E.; Morel, M. High proportion ZnO/CuO nanocomposites: Synthesis, structural and optical properties, and their photocatalytic behavior. *Surf. Interfaces* **2019**, *17*, 100367. [CrossRef]

69. Park, Y.; Yang, J.; Ryu, B.; Cho, J.; Cuong, T.; Hong, C.-H. Solution-processed multidimensional ZnO/CuO heterojunction as ultraviolet sensing. *Opt. Mater. Express* **2015**, *5*, 1752. [CrossRef]

70. Zou, W.; Zhang, L.; Liu, L.; Wang, X.; Sun, J.; Wu, S.; Deng, Y.; Tang, C.; Gao, F.; Dong, L. Engineering the Cu_2O-reduced graphene oxide interface to enhance photocatalytic degradation of organic pollutants under visible light. *Appl. Catal. B Environ.* **2016**, *181*, 495–503. [CrossRef]

71. Chen, C.; Liu, X.; Fang, Q.; Chen, X.; Liu, T.; Zhang, M. Self-assembly synthesis of CuO/ZnO hollow microspheres and their photocatalytic performance under natural sunlight. *Vacuum* **2020**, *174*, 109198. [CrossRef]

72. Prabhu, Y.; Rao, V.N.; Shankar, M.; Sreedhar, B.; Pal, U. The facile hydrothermal synthesis of CuO@ZnO heterojunction nanostructures for enhanced photocatalytic hydrogen evolution. *New J. Chem.* **2019**, *43*, 6794–6805. [CrossRef]

73. Tufa, L.; Oh, S.; Tran, V.; Kim, J.; Jeong, K.-J.; Park, T.; Kim, H.J.; Lee, J. Electrochemical immunosensor using nanotriplex of graphene quantum dots, Fe_3O_4, and Ag nanoparticles for tuberculosis. *Electrochim. Acta* **2018**, *290*, 369–377. [CrossRef]

74. Xu, H.; Fang, W.; Xu, L.; Liu, F. Batch Preparation of CuO/ZnO-Loaded Nanofiber Membranes for Photocatalytic Degradation of Organic Dyes. *Langmuir* **2020**, *36*, 14189–14202. [CrossRef]

75. Wei, Q.; Wang, Y.; Qin, H.; Wu, J.; Lu, Y.; Chi, H.; Yang, F.; Zhou, B.; Yu, H.; Liu, J. Construction of rGO wrapping octahedral Ag-Cu_2O heterostructure for enhanced visible light photocatalytic activity. *Appl. Catal. B Environ.* **2018**, *227*, 132–144. [CrossRef]

76. Guo, F.; Huang, X.; Chen, Z.; Cao, L.; Cheng, X.; Chen, L.; Shi, W. Construction of Cu3P-ZnSnO3-g-C3N4 p-n-n heterojunction with multiple built-in electric fields for effectively boosting visible-light photocatalytic degradation of broad-spectrum antibiotics. *Sep. Purif. Technol.* **2021**, *265*, 118477. [CrossRef]

77. Thatikayala, D.; Min, B. Ginkgo leaves extract-assisted synthesis of ZnO/CuO nanocrystals for efficient UV-induced photodegradation of organic dyes and antibacterial activity. *J. Mater. Sci. Mater. Electron.* **2021**, *32*, 17154–17169. [CrossRef]

78. Shaker-Agjekandy, S.; Habibi-Yangjeh, A. Microwave-assisted one-pot method for preparation of ZnO/AgI nanocomposites with highly enhanced photocatalytic activity under visible-light irradiation. *Desalin. Water Treat.* **2016**, *57*, 16015–16023. [CrossRef]

79. Fang, H.; Guo, Y.; Wu, T.; Liu, Y. Biomimetic synthesis of urchin-like CuO/ZnO nanocomposites with excellent photocatalytic activity. *New J. Chem.* **2018**, *42*, 12779–12786. [CrossRef]

80. Hayyan, M.; Hashim, M.; Alnashef, I. Superoxide Ion: Generation and Chemical Implications. *Chem. Rev.* **2016**, *116*, 3029–3085. [CrossRef]

81. Jenny, S.; Masaya, M.; Masato, T.; Jinlong, Z.; Yu, H.; Masakazu, A.; Detlef, W.B. Understanding TiO_2 photocatalysis: Mechanisms and materials. *Chem. Rev.* **2014**, *114*, 9919–9986.

82. Imangaliyeva, A.; Mastai, Y.; Seilkhanova, G. In situ synthesis and catalytic properties of Cu_2O nanoparticles based on clay materials and polyethylene glycol. *J. Nanoparticle Res.* **2019**, *21*, 97. [CrossRef]

83. Kandula, S.; Jeevanandam, P. Synthesis of Cu_2O@Ag Polyhedral Core-Shell Nanoparticles by a Thermal Decomposition Approach for Catalytic Applications. *Eur. J. Inorg. Chem.* **2016**, *2016*, 1548–1557. [CrossRef]

84. Zhao, Y.; Li, R.; Jiang, P.; Zhang, K.; Dong, Y.; Xie, W. Mechanistic Study of Catalytic Hydride Reduction of -NO_2 to -NH_2 Using Isotopic Solvent and Reducer: The Real Hydrogen Source. *J. Phys. Chem. C* **2019**, *123*, 15582–15588. [CrossRef]

85. Emiru, T.; Ayele, D. Controlled synthesis, characterization and reduction of graphene oxide: A convenient method for large scale production. *Egypt. J. Basic Appl. Sci.* **2017**, *4*, 74–79. [CrossRef]

86. Majumdar, D.; Baugh, N.; Bhattacharya, S. Ultrasound assisted formation of reduced graphene oxide-copper (II) oxide nanocomposite for energy storage applications. *Colloids Surf. A Physicochem. Eng. Asp.* **2017**, *512*, 158–170. [CrossRef]